*symmetry*

MDPI

*Article*

# Optical Bacteria Recognition: Cross-Polarized Scattering

**Riccardo Pepino, Hamed Tari, Alessandro Bile, Arif Nabizada and Eugenio Fazio ***

Dipartimento di Scienze di Base e Applicate per l'Ingegneria, Sapienza Università di Roma, 00161 Rome, Italy; riccardo.pepino@uniroma1.it (R.P.); hamed.tari@uniroma1.it (H.T.); alessandro.bile@uniroma1.it (A.B.); arif.nabizada@uniroma1.it (A.N.)

* Correspondence: eugenio.fazio@uniroma1.it

**Abstract:** The rapid identification of bacteria is extremely important for controlling infections and enabling swift and effective action. Light scattering has proven to be a highly versatile technique for identifying bacteria, as it does not require long colony growth times. In this article, we present a study on the use of cross-polarized optical scattering (CPS). Despite a relatively low scattering efficiency ($10^{-5}$ to $10^{-6}$), working with cross-polarization enhances contrast by eliminating a highly intense background of scattered light. CPS has been applied to four bacteria, with three similar in shape. Moreover, two of them are Gram+ and two Gram-. The obtained images have been reduced in size down to a 16-bit images and camera noise has been added. Although bacteria are symmetrical in principle, in reality rotations of their orientation generate asymmetries in the CPS patterns that were exploited precisely to recognize and classify the different species. The classification of bacteria by a t-SNE algorithm in a reduced-dimension space shows that their features are grouped into specific clusters. However, such classification is not completely decisive due to partial cluster overlapping.

**Keywords:** light scattering; cross-polarized scattering; light polarization; bacteria; bacterial detection; rapid testing

## 1. Introduction

Optical recognition of bacteria represents an emerging field at the intersection of microbiology, optical engineering, and artificial intelligence. This technology aims to quickly and accurately identify bacteria through the analysis of their optical characteristics, without the need for bacterial cultures, thereby reducing diagnostic times and improving the efficiency of medical, environmental, and industrial applications.

The potential applications of optical bacterial recognition are numerous. In the medical field, this technology could be used for the rapid diagnosis of bacterial infections [1] and for monitoring antibiotic resistance [2–4]. Traditionally, bacterial identification has relied on microbiological culture techniques, which, although accurate, require significant time and resources [5]. Recently, approaches based on optical technologies have gained attention for their ability to provide rapid and non-invasive results. These methods exploit the unique properties of bacteria, such as their cell shape, cell wall composition, and responses to specific light spectra [6].

Among the most commonly used optical technologies, there is advanced optical microscopy [7–12], flow cytometry [13–16], and Raman spectroscopy [17]. Raman spectroscopy, in particular, has been extensively studied for bacterial recognition due to its ability to detect the unique chemical fingerprints of bacteria. For example, it has been

check for updates

Academic Editor: Hao Xiong

Received: 23 January 2025
Revised: 27 February 2025
Accepted: 3 March 2025
Published: 6 March 2025

**Citation:** Pepino, R.; Tari, H.; Bile, A.; Nabizada, A.; Fazio, E. Optical Bacteria Recognition: Cross-Polarized Scattering. *Symmetry* **2025**, *17*, 396. https://doi.org/10.3390/sym17030396

**Copyright:** © 2025 by the authors. Licensee MDPI, Basel, Switzerland. This article is an open access article distributed under the terms and conditions of the Creative Commons Attribution (CC BY) license (https://creativecommons.org/licenses/by/4.0/).

demonstrated that Raman spectra can distinguish between different bacterial species and, in particular, can detect variations in the composition of proteins, lipids, and nucleic acids [17].

The main drawback of these techniques is their complexity, which is due to the instrumentation.

On the contrary, light scattering [17–21] has been successfully used for bacterial classification and has been shown to assess a bacterium's antimicrobial resistance [22]. It is a relatively simple technique that can be easily automated by combining it with classification algorithms. All this makes it easily portable, applicable even outside the laboratory with relative ease, and usable by less experienced personnel.

In this paper, we study Cross-Polarization Scattering (CPS), i.e., the interaction between polarized light and individual bacteria and the detection of the cross-polarization signal. Despite a relatively low efficiency ($10^{-5}$ to $10^{-6}$), working with CPS allows to us obtain good sensitivity by completely eliminating the unscattered residue.

## 2. Materials and Methods

### *2.1. Bacteria Structure*

Bacteria are prokaryotic organisms, that is, unicellular organisms whose genetic material is not enclosed within a specific membrane, and the compartmentalization of cellular functions in specific organelles is missing in the cytoplasm. Bacteria are divided into two macrogroups: Gram-positive (Gram+) and Gram-negative (Gram-), and their difference is based on the structure of their cell walls [5]. Gram+ bacteria have a cell wall made up of three layers: the first external layer of peptidoglycan, a small periplasma film [r], and an internal cell membrane, made up of phospholipids and proteins. Gram- bacteria instead have a complex cell wall made up of five layers: an external membrane, made up of phospholipids, proteins and lipopolysaccharides, a periplasma region, a thin layer of peptidoglycan, another thin layer of periplasma, and an internal cell membrane made up of phospholipids and proteins [5].

The cytoplasm of bacteria is a gelatinous solution that fills the inside of the cell, containing all of the components necessary for cellular functions, such as enzymes, nutrients, ribosomes and DNA. Although bacteria, unlike eukaryotes, do not have a nuclear membrane that encloses their genetic material, the DNA is mainly concentrated in a central region called the nucleoid [5].

In this work, we analyzed bacillus-shaped bacteria, i.e., rod-shaped, which are guaranteed to have an anisotropic shape and therefore can originate a characteristic diffusion of light. In particular, two Gram+ bacteria were analyzed (*Bacillus subtilis* and *Bacillus globigii*, also known as *Bacillus atrophaeus*) and two Gram- bacteria (*Bacillus salmonella* and *Cholera vibrio*). These bacilli have more or less the same shape, but differ in their size and membrane composition.

The scheme of the internal structures is shown in Figure 1, while in Table 1, the geometric parameters are reported.

**Table 1.** Geometric parameters of bacteria.

| Bacterium | GRAM | Radius | Length | Internal Membrane Thickness | External Membrane Thickness | Periplasmatic Thickness | Cytoplasm Radius | Nucleotide Length | Peptidoglycan Thickness |
|---|---|---|---|---|---|---|---|---|---|
| *Cholera* | Gram- | 215 nm [23] | 1.21 µm [24] | 10 nm [5] | 10 nm [5] | 15 nm [25] | 150 nm | 0.657 µm | - |
| *Salmonella* | Gram- | 375 nm [26] | 2.56 µm [26] | 8 nm [5] | 8 nm [5] | 15 nm [25] | 250 mm | 1.559 µm | - |
| *Subtilis* | Gram+ | 435 nm [27] | 2.3 µm [27] | 10 nm [5] | - | 22.3 nm [24] | 300 nm | 1.267 µm | 34 nm [22] |
| *Globigii* | Gram+ | 250 nm [28] | 2 µm [28] | 10 nm [5] | - | 22.3 nm [24] | 150 mm | 1.527 µm | 34 nm [22] |

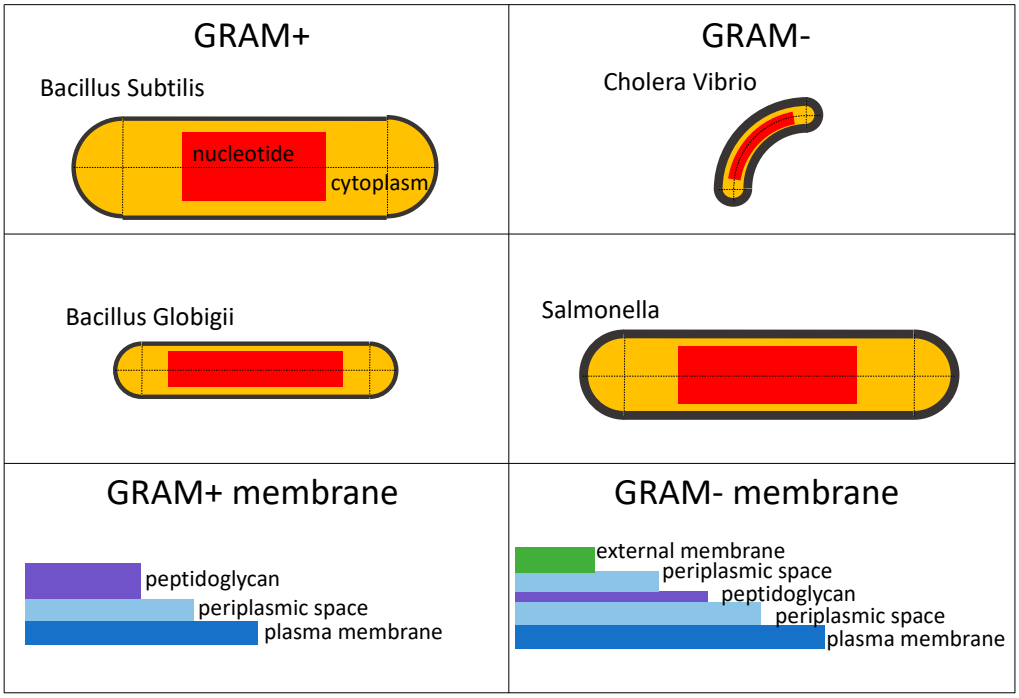



**Figure 1.** Schematic structure of Gram+ and Gram- bacteria.

### *2.2. Refractive Indices*

An important and indeed critical parameter in optical studies is the knowledge of the refractive indices of the various elements that make up the system. As bacteria are complex and non-homogeneous structures that are composed of many substances, the various elements of a bacterium can have different refractive indices due to their composition, thicknesses, and the concentration of water they contain. We have therefore carried out a detailed and in-depth evaluation of these refractive indices.

#### 2.2.1. Nucleotide

Using a non-absorbed wavelength, the internal composition of the cell can be considered to be approximately the same for all bacteria and, consequently, the associated refractive index is also the same [29]. For this reason, the nucleotide is the same for all of the analyzed bacteria and is mainly composed of RNA (with a nominal concentration of 0.5 g/mL), DNA (with a concentration of 6.8 g/mL), and proteins (with a concentration of 8.6 g/mL) [30]. To calculate its refractive index ($n_{NCT}$) we used the incremental formula [31], which describes the influence of the various components of the solution as a function of the concentration of the solutes:

$$n_{NCT} = n_0 + \sum_i \delta n_i \cdot c_i \quad (1)$$

where $n_0$ is the refractive index of the solvent, $\delta n_i$ are the index variations due to different concentrations of solutes $c_i$. Water with index $n_0$ =1.333 was used as solvent [32]; from the literature we find that $\delta n_{protein}$= 0.17 mL/gr [31], $\delta n_{RNA}$ = 0.20 mL/gr [33], and $\delta n_{DNA}$ = 0.16 mL/gr [34]. Consequently, $n_{NCT}$ = 1.3639 remains constant for all of the bacteria used.

#### 2.2.2. Cytoplasm

The cytoplasm was also analyzed within a non-absorptive spectral range; thus, its composition can be considered to be approximately identical across all of the bacteria examined. Consequently, its refractive index was uniformly calculated for all samples using the incremental Formula (1), based on the concentrations of the various compo-

nents. The macromolecular concentration within the cytoplasm ranges between 255 and 289 g/L [35–37]. Of this, approximately 60–68 g/L consists of RNA, with 9–10 g/L attributed to tRNA, and the remainder, amounting to 51–57.8 g/L, comprising ribosomal RNA. The protein component accounts for approximately 165–187 g/L, while a smaller fraction, ranging between 30 and 34 g/L, is composed of metabolites and polysaccharides.

Applying the incremental Formula (1), the refractive index of the cytoplasm was determined to lie between 1.3883 and 1.3935. This range is consistent with values reported in the literature, which approximate 1.39 [38,39].

#### 2.2.3. Bacterial Membrane

The calculation of the refractive index of the cell wall is complex since, as shown in Figure 1, bacterial cell walls of both Gram-positive and Gram-negative are multilayered structures that alternate components, such as peptidoglycan, periplasmic space, plasma membrane, and, in the case of Gram-negative bacteria, an additional outer membrane. For this reason, we first determined the refractive index of each region and then calculated an overall index as a weighted average of the multilayer structures, taking into account the thickness of each individual component.

##### Plasma and Outer Membranes

The plasma membrane and outer membrane are primarily composed of proteins and phospholipids in an approximate ratio of 4:6 [40]. However, the outer membrane of Gram-negative bacteria also contains lipopolysaccharides, located on the outermost surface [41].

The phospholipids and lipopolysaccharides present can vary in both the polar head and the length of the hydrophobic tail [5]. Depending on the polar head, they may include molecules, such as cardiolipin (CL), phosphatidylethanolamine (PE), phosphatidylglycerol (PG), lysophosphatidylethanolamine (LyslPE), lysophosphatidylglycerol (LysilPG), and diphosphatidylglycerol (DPG). Additionally, each phospholipid and lipopolysaccharide can have a hydrophobic tail composed of fatty acids of varying types and quantities. This variability means that membranes, while appearing structurally simple, exhibit highly diverse compositions, making their chemistry exploitable for bacterial identification [42]. To calculate the refractive index of the membranes, the Bruggeman Equation (5) [43,44] was used:

$$\sum_{i=1}^{m} f_i \frac{\varepsilon_i - \varepsilon_{eff}}{\varepsilon_i + 2 * \varepsilon_{eff}} + \sum_{i=1}^{m\prime} f_i \left( \sum_{j=1}^{3} \frac{\varepsilon_i - \varepsilon_{eff}}{\varepsilon_i + L_j * \left(\varepsilon_i - \varepsilon_{eff}\right)} \right) = 0 \quad (2)$$

which requires as inputs the volume fraction $f_i$ of each component, their dielectric constant $\varepsilon_i$, and, if necessary, the depolarization $L_j$. Regarding the volume fractions, the typical chemical compositions of various bacteria found in the literature [45–58] do not account for the presence of possible water molecules. However, molecular dynamics simulations reveal that, on average, 11.7 water molecules bind to each phospholipid head [53], while approximately 39 water molecules bind to each membrane protein [59]. Therefore, an accurate estimation of the volume fractions must consider water in the calculation of the chemical composition.

By initially approximating the membrane mass as the product of the effective density and the membrane volume as follows:

$$m_{membrane} = \rho_{effective} \cdot vol \quad (3)$$

and assuming the additivity of volumes, the effective density can be calculated using the following relationship:

$$\rho_{effective} = m_{tot} \sum_i \frac{\rho_i}{m_i} = \sum_i \frac{\rho_i}{c_i} \quad (4)$$

where $c_i$ represents the concentrations. From the effective density, the total mass and the mass of individual components are calculated, which are then used to determine the number of moles of each macromolecule and, consequently, the number of water molecules bound to the membrane. Subsequently, using the newly calculated concentrations, the volume fractions for each component were obtained. The values of the dielectric constants and the densities of the various macromolecules [60–64] are listed in Table 2.

**Table 2.** Density and refractive index values of membrane components.

| | PE | PG | CL | LPS | MP | NL | DPG | LYSOPE | LPG | RNA | DNA | DAG | DGDG | $H_2O$ |
|---|---|---|---|---|---|---|---|---|---|---|---|---|---|---|
| $\rho$ | 1.3 | 1.3 | 1.6 [r] | 1.1 | 1.32 | 0.9 | 1.6 | 1.1 | 1.4 | 2 | 1.4 | 0.9 | 1.5 | 1 |
| $n$ | 1.475 | 1.475 | 1.505 | 1.512 | 1.621 | 1.480 | 1.460 | 1.527 | 1.533 | 1.635 | 1.587 | 1.472 | 1.590 | 1.3337 |

Phospholipids can be considered cylindrical in shape and are therefore anisotropic, necessitating the calculation of the depolarization factor $L_j$. To this end, they were modeled as randomly oriented cylinders, with a length equal to half the thickness of the membrane and a cross-sectional area of 0.65 $nm^2$ [53]. Similarly, lipopolysaccharides, when present, were treated analogously but with a cross-sectional area of 2.32 $nm^2$ [65].

The refractive index ranges for each membrane are reported in Table 3. As can be observed, these values fall within the expected range of 1.35–1.60, as documented in the literature [39,40,66–68].

**Table 3.** Calculated refractive indices for the cell wall and its components.

| Bacterium | External Membrane | Peptidoglycan | Periplasm | Internal Membrane | Cell Wall |
|---|---|---|---|---|---|
| *Salmonella* | 1.50–1.55 | - | 1.35–1.37 | 1.52–1.53 | 1.43–1.45 |
| *Vibrio cholera* | 1.52–1.54 | - | 1.34–1.36 | 1.52–1.53 | 1.45–1.46 |
| *Bacillus subtilis* | - | 1.351 | 1.35–1.36 | 1.54–1.59 | 1.38–1.39 |
| *Bacillus globigii* | - | 1.351 | 1.35–1.36 | 1.54–1.59 | 1.38–1.39 |

Periplasm

The refractive index of the periplasm was calculated using Equation (1). For *Vibrio cholerae* and *Salmonella*, the thin peptidoglycan layer was considered as a solute within the periplasm, and the values reported in [69] were used. For bacilli, the values provided in [70] were employed. The maximum and minimum values obtained are shown in Table 3.

Peptidoglycan

Finally, the refractive index of the thick peptidoglycan layer in bacilli is 1.351, as reported in [71].

2.2.4. Membrane Refractive Indices

Once the refractive index values for the various membrane compartments were determined, the overall refractive index $n_{tot}$ of the cell wall was calculated (Table 3) as the weighted average based on the thicknesses $S_i$ of the individual walls:

$$\text{GRAM}-: \quad n_{tot}s_{tot} = n_{om}s_{om} + n_{per}s_{per} + n_{im}s_{im} \quad (5)$$

$$\text{GRAM+}: \quad n_{tot}s_{tot} = n_{pep}s_{pep} + n_{per}s_{per} + n_{im}s_{im} \tag{6}$$

### *2.3. Numerical Simulation Model*

The light scattering by bacteria was simulated using the COMSOL Multiphysics software (v. 6.2) with the Wave Optics module. The 3D models were divided into nucleoid, cytoplasm, and cell wall, with different characteristics for Gram-negative and Gram-positive bacteria (see Table 1). In the model, individual bacteria (Figure 2) are positioned within water cylinders with their axis parallel to the $x$-axis, which also corresponds to the propagation direction of a plane wave with a wavelength of 532 nm, linearly polarized along the $z$-axis. The cylinders represent the numerical integration volumes for the scattered electromagnetic field.

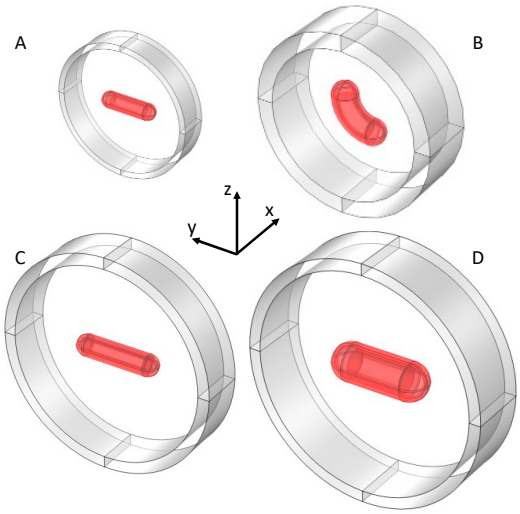



**Figure 2.** Three-dimensional models of individual bacteria. (**A**) *Salmonella enterica*. (**B**) *Vibrio cholerae*. (**C**) *Bacillus globigii*. (**D**) *Bacillus subtilis*.

The walls of the cylinders were designed to be at a distance of at least $\lambda/2$ from the bacterium (which is why the cylinders have different dimensions), to prevent the absorption of scattered field components that could affect the diffraction image. At the edges of the cylinder, a Perfectly Matched Layer (PML) with a thickness of $\lambda/2$ was applied to control spurious numerical reflections. In the simulation of the system, variable tetrahedral meshes were employed, with a maximum size of $\frac{\lambda}{5n_i}$.

The numerical model simulates the interaction between vertically polarized radiation (z-polarization) and an anisotropic object, which is the bacterium. First, it solves Maxwell's equations within a cylinder to determine the component of polarization converted to the horizontal (y-polarization). Subsequently, this component is propagated using the Fresnel equation under the near-field approximation:

$$I_y(y,z) = \frac{1}{\Omega}\left|\frac{1}{i\lambda d}\iint E_y(u,v)e^{-i\frac{\pi}{\lambda X}(y^2+z^2)}e^{i\frac{2\pi}{\lambda X}(uy+zv)}dv\,du\right|^2 \tag{7}$$

where X represents the propagation distance and $\Omega$ s the electromagnetic impedance of the vacuum.

Several simulations were conducted, varying the refractive index between its maximum and minimum values for each region and modifying, as shown in Figure 3, the orientation of the bacterium both around the propagation axis and the angle relative to the xz plane. In this way, 720 images were generated for each bacterium, resulting in a total of 2880 images.

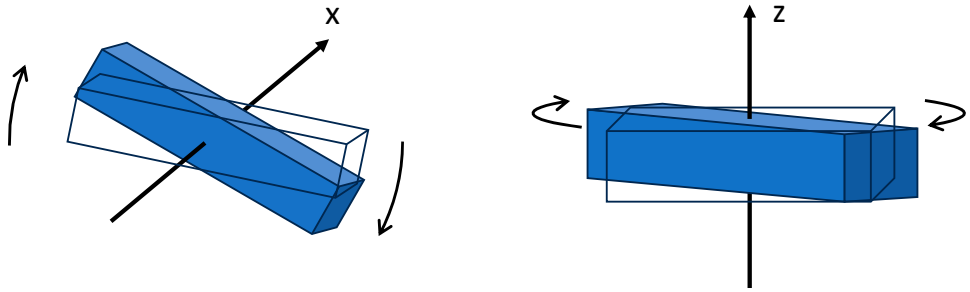



**Figure 3.** The simulations were performed by rotating the bacteria around the *x* and *z* axes to capture all possible orientations.

## 3. Results

### *3.1. Cross-Polarization Scattering Images Generated by Rotating the Bacteria Around the x-Axis*

Initially, we simulated the scattering of linearly polarized light along the *z*-axis in the far field by rotating the bacteria around the *x*-axis, which corresponds to the propagation axis of the light. Figure 4 shows the intensity maps for y-polarization obtained for *Salmonella* and *Vibrio cholerae* bacteria for rotations ranging from 0° to 170°. As can be observed, the two maps are distinctly different due to the differing morphology of the bacteria. The CPS efficiency was estimated to be on the order of $10^{-5} \div 10^{-6}$. The maximum scattering efficiency was observed for bacterial rotations near 45°/135°, where the coupling between the two cross-polarizations is most efficient.

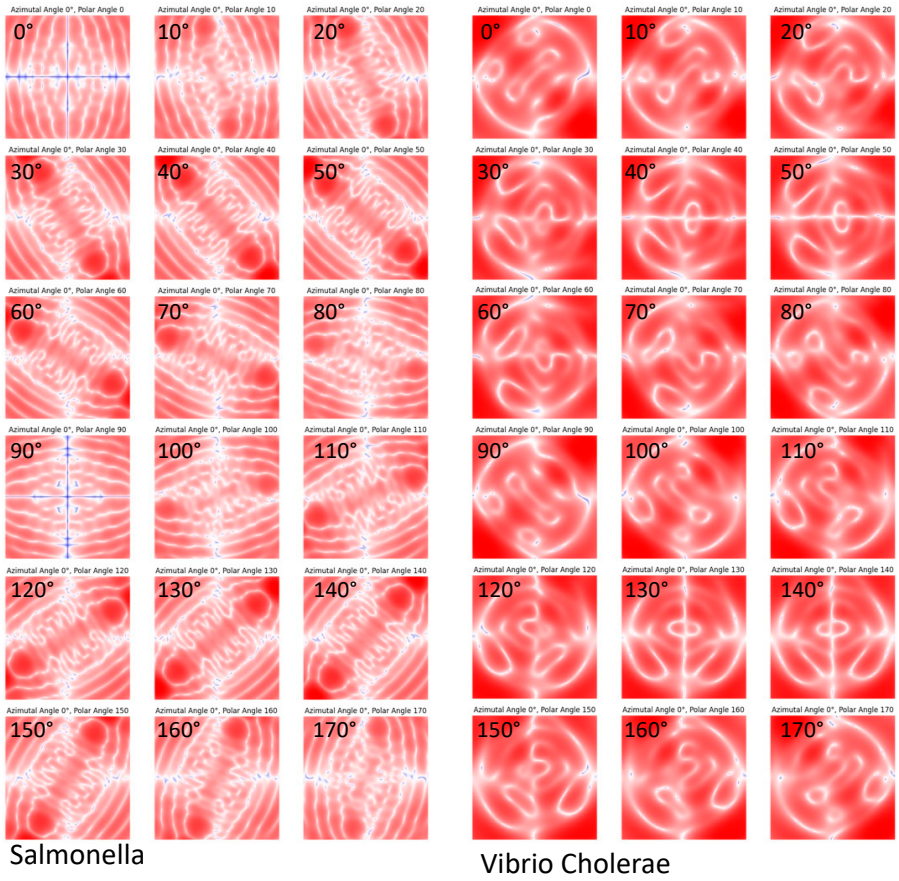



**Figure 4.** CPS maps for *Salmonella* and *Vibrio cholerae* bacteria for rotations from 0° to 170° around the x-axis (blue color corresponds to zero light intensity).

Figure 5 presents a comparison of the normal-incidence images (x-angle 0°, z-angle 0°) for *Salmonella* and the two bacilli, as they produce diffraction patterns with similar charac-

teristics due to their similar geometric structures. Despite their similar morphology, the differing membranes and biochemical compositions render them optically distinct.

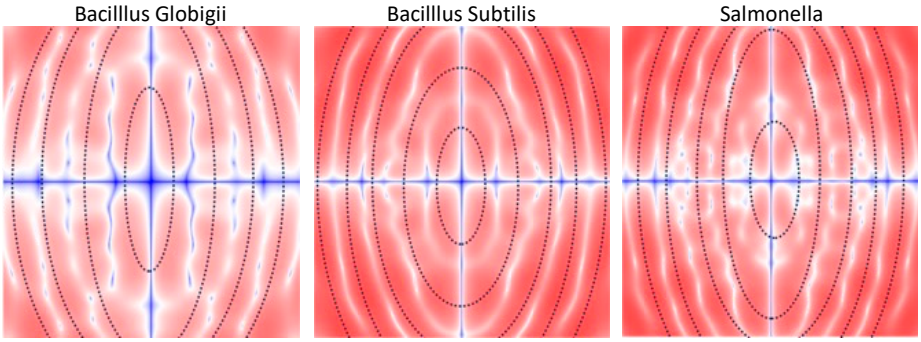



**Figure 5.** Cross-polarized optical scattering (CPS) images for *Salmonella* and *Bacilli* (*globigii* and *subtilis*) bacteria at normal incidence. Images display concentric elliptical structures (dashed lines), whose dimensions depend on size of bacteria (blue color corresponds to zero light intensity).

The images exhibit symmetry with respect to any axis passing through their center. Specifically, the two resulting halves are identical but rotated by 180° relative to each other. Additionally, they display concentric ellipses (dashed lines in the figure), with the shorter radius aligned along the horizontal direction and the longer radius parallel to the vertical direction, resulting in a 90° rotation compared to the original orientation of the bacteria. This rotation can be explained by drawing a parallel with diffraction through a rectangular slit: light tends to diverge more along the direction of the smaller axis [72]. Similarly, in the case of bacteria, their geometry leads to broader diffraction along the shorter axis, generating ellipses that vary in number and size based on the geometric characteristics of the bacteria.

Finally, the intensity of the diffraction images progressively increases from the center toward the edges, indicating that the higher spatial frequencies of the object contribute more significantly to light scattering and polarization conversion. This trend partially depends on the exposed surface area: larger bacteria, such as *Bacillus subtilis*, scatter more light than smaller bacteria, such as *Bacillus globigii*, due to greater interaction with the incident radiation. However, the intensity differences observed between bacteria of similar sizes, such as *Bacillus subtilis* and *Salmonella*, are attributable to the refractive index. *Salmonella*, having a higher refractive index, amplifies the intensity of the peaks without altering the shape of the diffraction pattern, thereby converting light polarization more efficiently.

Figure 6b,d show the images of *Vibrio cholerae* with rotations around the $x$-axis of 0° and 45°. At a zero angle, the image exhibits characteristics similar to those of *Salmonella* at 45°, with peaks distributed along an axis inclined at −45° relative to the center of the image and clear symmetry along this axis. This occurs because, as shown in Figure 6a, *Vibrio cholerae* is aligned along an axis inclined at 45°. Rotating it by 45°, as in Figure 6c, aligns it along the vertical axis, producing a pattern similar to those of the other bacteria, albeit with some differences. The *Vibrio cholerae* pattern is symmetric only along the horizontal axis. Additionally, although it has geometric parameters similar to other bacteria, its intrinsic curvature compacts its geometric dimensions compared to others, resulting in a greater angular divergence of light. Consequently, its diffraction patterns exhibit broader and fewer peaks, mostly confined to those near the center, with overall lower intensity compared to other bacteria.

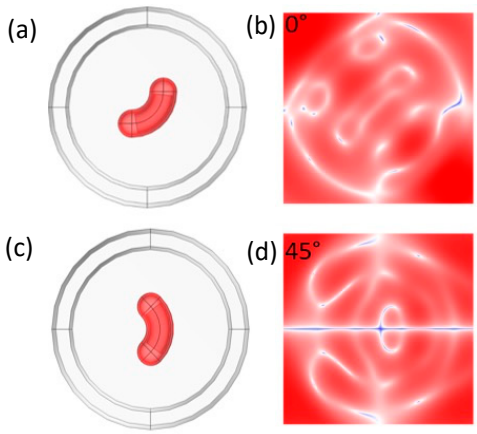



**Figure 6.** Orientations (**a**,**c**) and corresponding CPS images (**b**,**d**) for *Vibrio cholerae* at angles around the *x*-axis of 0° and 45° (blue color corresponds to zero light intensity).

### *3.2. Cross-Polarization Scattering Images Generated by Rotating the Bacteria Around the z-Axis*

Figure 7 presents a comparison of the CPS intensity maps for the four bacteria, obtained at the angles x:0°/z:0°, x:90°/z:0°, and x:0°/z:90°. The images corresponding to x:90°/z:0° are simply rotated by 90 degrees relative to those at x:0°/z:0°, which were previously analyzed, and exhibit similar characteristics. In contrast, the images for x:0°/z:90° demonstrate different behaviors. For *Salmonella* and the bacilli, the patterns exhibit radial symmetry and resemble those obtained from spherical objects or objects with circular cross-sections. The distribution of the peaks follows a trend similar to that observed at a zero x-angle, directly depending on the radial size of the object and increasing as this dimension grows.

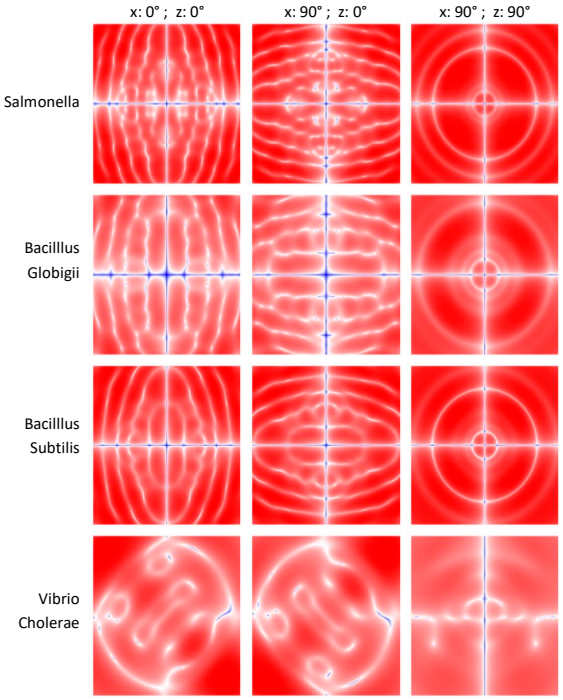



**Figure 7.** Comparison of CPS images of the four bacteria for 90° rotations around the main axes *x* and *z* (blue color corresponds to zero light intensity).

In the case of *Vibrio cholerae*, a different trend is observed. Due to its curvature, its structure closely resembles that of rod-shaped bacteria with a z-angle of 45°, and consequently, its diffraction patterns are very similar to theirs.

### *3.3. CPS Images Generated by Varying the Refractive Indices Between the Calculated Maximum and Minimum Values*

CPS signals exhibit some variability in the refractive index values of the membranes for both Gram-positive and Gram-negative bacteria. The influence of the refractive index on the intensity mapping of cross-polarized scattered light is shown in Figure 8. As observed, variations in the refractive index do not alter the geometry of the mapping but only its contrast, making the peaks and valleys more or less pronounced. This allowed us to simplify the image analysis, maintaining the information obtained for one refractive index equivalent to that of another.

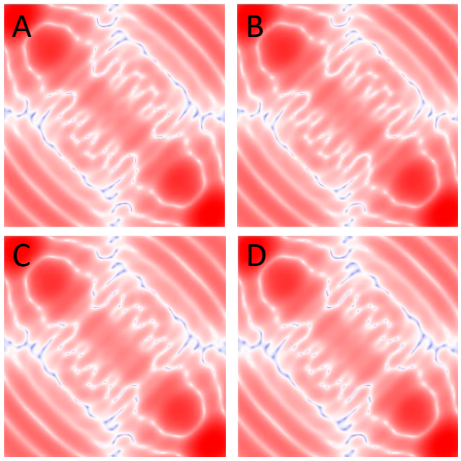



**Figure 8.** *Salmonella* bacterium: x-angle of 45°, z-angle of 0°. Variation in CPS images for the refractive index values of the membranes as reported in Table 3: (**A**) $n_{cit} = 1.3883, n_{memb} = 1.43$; (**B**) $n_{cit} = 1.3883, n_{memb} = 1.45$; (**C**) $n_{cit} = 1.3935, n_{memb} = 1.43$; and (**D**) $n_{cit} = 1.3935, n_{memb} = 1.45$. (blue color corresponds to zero light intensity).

## 4. Discussion

### *4.1. 16-Bit Image Reduction and the t-SNE Algorithm for Reducing the Information Dimension*

To simulate real-world behavior, we converted the obtained mappings to a 16-bit dynamic range, which is typical of most commercial cameras. In doing so, we considered a quantum efficiency of 0.8, which is standard for 16-bit cameras [r]. The images obtained using this procedure are shown in Figure 9. In this case as well, it was observed that three of the classes appear very similar, while the fourth is distinctly different.

The most evident characteristic of the transformed images is the marked difference that persists among them: at the same refractive index, the images of the bacteria remain distinct, reflecting their unique structural properties. However, the discretization—necessary because the number of photons cannot be a decimal value—leads to the elimination of many peaks that are present in the original images. This effect is particularly noticeable for polar angles that are multiples of 90° or equal to 0°: under these conditions, some peaks are significantly flattened, and the images are characterized by a few dominant peaks. Despite the reduction in the amount of information contained in the images, the 16-bit transformation preserves the main features required to analyze the differences between the bacteria and for their potential classification. For instance, a possible numerical approach to extracting new information from the mappings, making them unique and distinguishable, can be achieved by applying a dimensionality reduction using the nonlinear t-SNE (t-distributed Stochastic Neighbor Embedding) algorithm.

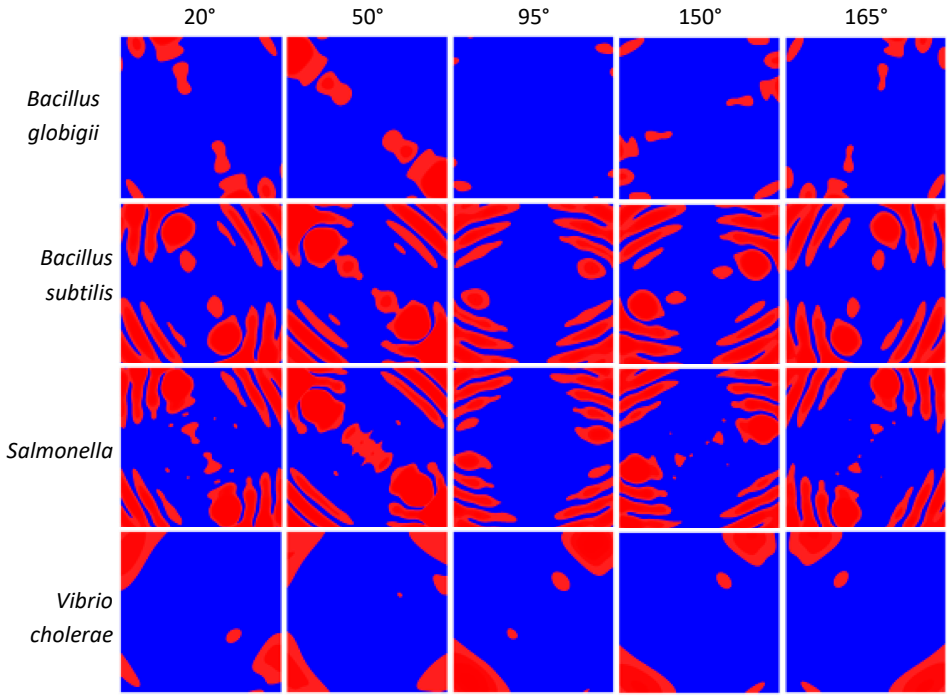
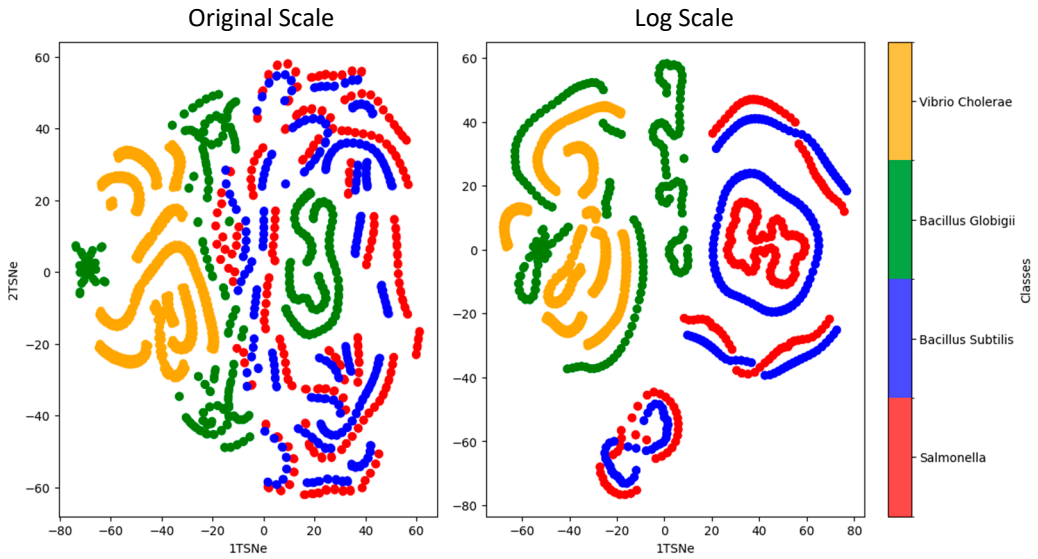



**Figure 9.** 16-bit CPS images (all with same orientation at z = 0°). (blue color corresponds to zero light intensity).

### *4.2. Application of the t-SNE Algorithm for Reducing the Information Dimension*

The obtained images are all different from each other, due to different orientations or different bacteria. The variation between the bacteria is a positive aspect because it favors recognition. The problem arises with the similarities, for example, in images belonging to the same bacterium but at different orientations. Moreover, images have extremely complex characteristics, which is indeed not very intuitive for direct observation. To better manage the large amount of information derived from these images, we applied the t-SNE algorithm to reduce multidimensional vectors (such as images) to a lighter space where image differences can be easily highlighted. Therefore, the t-SNE algorithm allows us to represent a very large dataset in a reduced space in order to qualitatively estimate the different characteristics of the data and therefore of the scattering sources.

The nonlinear t-SNE algorithm is an unsupervised neural technique for dimensionality reduction: it separates dissimilar information (representing it as distant points with a low probability on a new two-dimensional map) and clusters similar information (representing it as closely grouped points with a high probability). We have applied the t-SNE algorithm to the 2880 images obtained from the CPS simulations, whose results are shown in Figure 10A. The algorithm mapped the CPS intensity distributions into a lower-dimensional space while preserving the pairs of points with a high similarity. Using this technique, the *Vibrio cholerae* cluster is localized in a well-defined region, completely separated from the others. *Bacillus globigii* forms small distinct clusters, while the *Salmonella* and *Bacillus subtilis* classes almost entirely overlap. This makes it challenging to define a curve that precisely distinguishes the four classes. Indeed, we anticipate good classification performance for *Vibrio cholerae*, given its clear separation from the other classes. *Bacillus globigii* is expected to be classified with moderate accuracy, thanks to the formation of small clusters. In contrast, distinguishing between *Salmonella* and *Bacillus subtilis* is problematic: the points in both classes follow similar and closely aligned trajectories, making their differentiation complex.




(**A**) (**B**)

**Figure 10.** (**A**) TSNe normal images and (**B**) TSNe logarithmic scale images.

When a logarithmic transformation of the images is applied, it can be observed that although the t-SNE representation appears different (Figure 10B), it retains the same characteristics as the one obtained with untransformed images, while enhancing the positional differentiation between the bacteria. Using the logarithmic-scale t-SNE representation, not only does *Vibrio cholerae* exhibit a unique mapping position, but *Bacillus globigii* also becomes distinguishable from the others. For *Salmonella* and *Bacillus subtilis*, however, the maps show significant overlaps that necessitate the use of artificial intelligence techniques for discrimination [73]. Thus, this representation is able to discriminate different species by identifying clusters of typical features. Such classification has proven, however, not to be completely conclusive, requiring more sophisticated techniques to resolve the conflicts.

To further contextualize our findings, we compared the performance of CPS with other optical bacterial recognition techniques, such as Raman spectroscopy and flow cytometry. Raman spectroscopy provides detailed molecular fingerprints of bacteria and has been extensively studied for bacterial recognition due to its ability to detect unique biochemical signatures [17]. However, its application in real-time diagnostics is limited by the need for complex instrumentation and extensive post-processing [17]. On the other hand, flow cytometry enables rapid classification of bacterial populations and has been successfully applied in bacterial identification [13–16], but it often requires fluorescent labeling, making it less suited for label-free applications [13]. CPS, despite its relatively low scattering efficiency ($10^{-5}$ to $10^{-6}$), offers the advantage of background suppression, significantly improving the signal-to-noise ratio without requiring external markers. The preliminary classification using the t-SNE algorithm demonstrates that CPS can capture structural differences in bacterial morphologies, though partial cluster overlap indicates that further optimization is required. These results suggest that CPS, when integrated with machine learning techniques, could provide a balance between speed, simplicity, and accuracy in bacterial identification, complementing existing methodologies in scenarios where label-free, rapid screening is required.

## 5. Conclusions

In this paper, we show that Optical Cross-Polarized Scattering can be an effective and rapid technique for bacterial recognition. The technique provided a very large dataset of

images from the same bacterium or from different bacteria useful for the purpose of characterization and classification. To reduce the amount of data without losing information, we used the t-SNE algorithm, which allowed us to group all of the data into a single map to compare them. This application allowed the data to cluster into ensemble of characteristics of single bacteria and thus make them identifiable within reduced-dimensional maps. However, this representation has not proven to be conclusive because of several overlapping clusters caused by the extreme variability of the data. This study has highlighted the need to use more complex classification codes, for example, with the direct use of machine learning techniques.

**Author Contributions:** Conceptualization, E.F. and R.P.; software, R.P., H.T., A.N. and A.B.; formal analysis, R.P. and E.F.; investigation, E.F. and R.P.; writing—review and editing, E.F. and R.P.; supervision, E.F.; funding acquisition, R.P. and E.F.; revision R.P., E.F. and A.B. All authors have read and agreed to the published version of the manuscript.

**Funding:** Sapienza Università di Roma—Avvio alla Ricerca (B83C23004760001). Sapienza Università di Roma—Avvio alla Ricerca (AR224190029D8129).

**Data Availability Statement:** Data are available upon request.

**Acknowledgments:** The authors are indebted to M. Iodice of ISASI-CNR for the use of the COMSOL Multiphysics program machine time.

**Conflicts of Interest:** The authors declare no conflicts of interest.

## References

1. Harding, S.E. Applications of light scattering in microbiology. *Biotechnol. Appl. Biochem.* **1986**, *8*, 489–509. [PubMed]
2. Brown, C.; Tseng, D.; Larkin, P.M.K.; Realegeno, S.; Mortimer, L.; Subramonian, A.; Di Carlo, D.; Garner, O.B.; Ozcan, A. An Automated, Cost-Effective Optical System for Accelerated Anti-Microbial Susceptibility Testing (AST) Using Deep Learning. *arXiv* **2020**, arXiv:2005.11454.
3. Normani, S.; Bertolotti, P.; Bisio, F.; Magnozzi, M.; Carboni, F.F.; Filattiera, S.; Perotto, S.; Marangi, F.; Lanzani, G.; Scotognella, F.; et al. Tamm Plasmon Resonance as Optical Fingerprint of Silver/Bacteria Interaction. *arXiv* **2022**, arXiv:2212.05287. [CrossRef]
4. Kim, G.; Jo, Y.; Cho, H.; Choi, G.; Kim, B.-S.; Min, H.-S. Automated Identification of Bacteria Using Three-Dimensional Holographic Imaging and Convolutional Neural Network. In Proceedings of the 2018 IEEE Photonics Conference (IPC), Reston, VA, USA, 30 September–4 October 2018; pp. 1–2.
5. Madigan, M.T.; Bender, K.S.; Buckley, D.H.; Sattley, W.M.; Stahl, D.A. *Brock Biology of Microorganisms*; Pearson: New York, NY, USA, 2018.
6. Jenkins, C.; Cooper, J.; Smith, A. Optical methods for bacterial identification: A review. *J. Microbiol. Methods* **2020**, *178*.
7. Wang, A.; Garmann, F.R.; Manoharan, N.V. Tracking *E. coli* runs and tumbles with scattering solutions and digital holographic microscopy. *Opt. Express* **2016**, *24*, 23719–23725. [CrossRef] [PubMed]
8. Vater, S.M.; Weiße, S.; Maleschlijski, S.; Lotz, C.; Koschitzki, F.; Schwartz, T.; Obst, U.; Rosenhahn, A. Swimming Behavior of *Pseudomonas aeruginosa* Studied by Holographic 3D Tracking. *PLoS ONE* **2014**, *9*, e87765. [CrossRef]
9. Oh, J.; Ryu, J.S.; Lee, M.; Jung, J.-H.; Han, S.; Chung, H.J.; Park, Y. Three-dimensional label-free observation of individual bacteria upon antibiotic treatment using optical diffraction tomography. *Biomed. Opt. Express* **2020**, *11*, 1257–1267. [CrossRef] [PubMed]
10. Gopinath, S.C.; Tang, T.-H.; Chen, Y.; Citartan, M.; Lakshmipriya, T. Bacterial detection: From microscope to smartphone. *Biosens. Bioelectron.* **2014**, *60*, 332–342. [CrossRef]
11. Buzalewicz, I.; Kujawińska, M.; Krauze, W.; Podbielska, H. Novel Perspectives on the Characterization of Species-Dependent Optical Signatures of Bacterial Colonies by Digital Holography. *PLoS ONE* **2016**, *11*, e0150449. [CrossRef]
12. Bedrossian, M.; El-Kholy, M.; Neamati, D.; Nadeau, J. A Machine Learning Algorithm for Itdentifying and Tracking Bacteria in Three Dimensions using Digital Holographic Microscopy. *AIMS Biophys.* **2018**, *5*, 36–49. [CrossRef]
13. Ou, F.; McGoverin, C.; White, J.; Swift, S.; Vanholsbeeck, F. Bead-Based Flow-Cytometric Cell Counting of Live and Dead Bacteria. *Methods Mol. Biol.* **2019**, *1968*, 123–134. [PubMed]
14. Galazzo, G.; van Best, N.; Benedikter, B.J.; Janssen, K.; Bervoets, L.; Driessen, C.; Oomen, M.; Lucchesi, M.; van Eijck, P.H.; Becker, H.E.F.; et al. How to Count Our Microbes? The Effect of Different Quantitative Microbiome Profiling Approaches. *Front. Cell. Infect. Microbiol.* **2020**, *10*, 403. [CrossRef] [PubMed]

15. Haridas, V.; Ranjbar, S.; Vorobjev, I.A.; Goldfeld, A.E.; Barteneva, N.S. Imaging flow cytometry analysis of intracellular pathogens. *Methods* **2017**, *112*, 91–104. [CrossRef]
16. Johansson, J.; Karlsson, A.; Bylund, J.; Welin, A. Phagocyte interactions with *Mycobacterium tuberculosis*—Simultaneous analysis of phagocytosis, phagosome maturation and intracellular replication by imaging flow cytometry. *J. Immunol. Methods* **2015**, *427*, 73–84. [CrossRef] [PubMed]
17. Stöckel, S.; Kirchhoff, J.; Heinemann, S.H. Raman spectroscopy for bacterial identification. *Clin. Chem.* **2015**, *61*, 89–98.
18. He, Y.; Reed, S.; Bhunia, A.K.; Gehring, A.; Nguyen, L.-H.; Irwin, P.L. Rapid identification and classification of *Campylobacter* spp. using laser optical scattering technology. *Food Microbiol.* **2015**, *47*, 28–35. [CrossRef]
19. Wang, P.; Sun, H.; Yang, W.; Fang, Y. Optical Methods for Label-Free Detection of Bacteria. *Biosensors* **2022**, *12*, 1171. [CrossRef]
20. Romphosri, S.; Pissuwan, D.; Wattanavichean, N.; Buabthong, P.; Waritanant, T. Rapid alignment-free bacteria identification via optical scattering with LEDs and YOLOv8. *Sci. Rep.* **2024**, *14*, 20498. [CrossRef]
21. Iyengar, S.N.; Dowden, B.; Ragheb, K.; Patsekin, V.; Rajwa, B.; Bae, E.; Robinson, J.P. Identifying antibiotic-resistant strains via cell sorting and elastic-light-scatter phenotyping. *Appl. Microbiol. Biotechnol.* **2024**, *108*, 406. [CrossRef]
22. Weart, R.B.; Lee, A.H.; Chien, A.-C.; Haeusser, D.P.; Hill, N.S.; Levin, P.A. A metabolic sensor governing cell size in bacteria. *Cell* **2007**, *130*, 335–347. [CrossRef]
23. Zuber, B.; Haenni, M.; Ribeiro, T.; Minnig, K.; Lopes, F.; Moreillon, P.; Dubochet, J. Granular Layer in the Periplasmic Space of Gram-Positive Bacteria and the Fine Structures of *Enterococcus gallinarum* and *Streptococcus gordonii* Septa Revealed by Cryo-Electron Microscopy of Vitreous Sections. *J. Bacteriol.* **2006**, *188*, 6652–6660. [CrossRef]
24. Bernard, K.; Wormser, G.P. Biodefense Principles and Pathogens Edited By M. S. Bronze and R. A. Greenfield Norfolk, United Kingdom: Horizon Bioscience, 2005. 838 pp. *Clin. Infect. Dis.* **2006**, *42*, 735. [CrossRef]
25. Sun, J.; Rutherford, S.T.; Silhavy, T.J.; Huang, K.C. Physical properties of the bacterial outer membrane. *Nat. Rev. Microbiol.* **2022**, *20*, 236–248. [CrossRef]
26. Fàbrega, A.; Vila, J. Salmonella enterica Serovar Typhimurium Skills To Succeed in the Host: Virulence and Regulation. *Clin. Microbiol. Rev.* **2013**, *26*, 308–341. [CrossRef] [PubMed]
27. Pasquina-Lemonche, L.; Burns, J.; Turner, R.D.; Kumar, S.; Tank, R.; Mullin, N.; Wilson, J.S.; Chakrabarti, B.; Bullough, P.A.; Foster, S.J.; et al. The architecture of the Gram-positive bacterial cell wall. *Nature* **2020**, *582*, 294–297. [CrossRef]
28. Available online: https://bacdive.dsmz.de/strain/1077 (accessed on 2 March 2025).
29. Myers, J.A.; Curtis, B.S.; Curtis, W.R. Improving accuracy of cell and chromophore concentration measurements using optical density. *BMC Biophys.* **2013**, *6*, 4. [CrossRef] [PubMed]
30. Valkenburg, J.A.; Woldringh, C.L. Phase separation between nucleoid and cytoplasm in Escherichia coli as defined by immersive refractometry. *J. Bacteriol.* **1984**, *160*, 1151–1157. [CrossRef]
31. Barer, R.; Joseph, S. Refractometry of Living Cells. *Nature* **1953**, *171*, 399–423. [CrossRef]
32. Hale, G.M.; Querry, M.R. Optical constants of water in the 200-nm to 200-µm wavelength region. *Appl. Opt.* **1973**, *12*, 555–563. [CrossRef]
33. Zhao, H.; Brown, P.H.; Schuck, P. On the Distribution of Protein Refractive Index Increments. *Biophys. J.* **2011**, *100*, 2309–2317. [CrossRef]
34. Scafati, A.R.; Stornaiuolo, M.R.; Novaro, P. Physicochemical and Light Scattering Studies on Ribosome Particles. *Biophys. J.* **1971**, *11*, 370–384. [CrossRef] [PubMed]
35. de Jong, H.; Casagranda, S.; Giordano, N.; Cinquemani, E.; Ropers, D.; Geiselmann, J.; Gouzé, J.-L. Mathematical modelling of microbes: Metabolism, gene expression and growth. *J. R. Soc. Interface* **2017**, *14*, 20170502. [CrossRef] [PubMed]
36. Zimmerman, S.B.; Trach, S.O. Estimation of macromolecule concentrations and excluded volume effects fort the cytoplasm of *Escherichia coli*. *J. Mol. Biol.* **1991**, *222*, 599–620. [CrossRef]
37. McGueffee, S.R.; Elcock, A.H. Diffusion, Crowding & Protein Stability in a Dynamic Molecular Model of the Bacterial Cytoplasm. *PLoS Comput. Biol.* **2010**, *6*, e1000694.
38. Ross, K.F.A.; Billing, E. The Water and Solid Content of Living Bacterial Spores and Vegetative Cells as Indicated by Refractive Index Measurements. *J. Gen. Microbiol.* **1957**, *16*, 418–425. [CrossRef]
39. Suhling, K.; Siegel, J.; Phillips, D.; French, P.M.; Lévêque-Fort, S.; Webb, S.E.; Davis, D.M. Imaging the Environment of Green Fluorescent Protein. *Biophys. J.* **2002**, *83*, 3589–3595. [CrossRef]
40. Goodsell, D.S. Inside a living cell. *Trends Biochem. Sci.* **1991**, *16*, 203–206. [CrossRef]
41. Funahara, Y.; Nikaido, H. Asymmetric Localization of Lipopolysaccharides on the Outer Membrane of *Salmonella typhimurium*. *J. Bacteriol.* **1980**, *141*, 1463–1465. [CrossRef] [PubMed]
42. Prescott, L.M. *Microbiology*; Mcgraw-Hill: New York, NY, USA, 2002.
43. Sihvola, A. *Electromagnetic Mixing Formulas and Applications*; Electromagnetic Waves Series; IET: London, UK, 1999.
44. Goncharenko, A.V. Generalizations of the Bruggeman equation and a concept of shape-distributed particle composites. *Phys. Rev. E* **2004**, *68*, 041108. [CrossRef]

45. Ames, G.F. Lipids of Salmonella Typhirium and Escherichia coli: Structure and Metabolism. *J. Bacteriol.* **1968**, *95*, 833–843. [CrossRef]
46. Smit, J.; Kamio, Y.; Nikaido, H. Outer Membrane of *Salmonella typhimurium*: Chemical Analysis and Freeze-Fracture Studies with Lipopolysaccharide Mutants. *J. Bacteriol.* **1976**, *124*, 942–958. [CrossRef]
47. Jones, N.C.; Osborn, M.J. Tranlocation of Phospholipids between the Outer and Inner Membranes of *Salmonella typhimurium*. *J. Biol. Chem.* **1977**, *252*, 7405–7412. [CrossRef]
48. Rana, F.R.; Sultany, C.M.; Blazyk, J. Determination of the lipid composition of *Salmonella typhimurium* outer membranes by 31P NMR. *J. Microbiol. Methods* **1991**, *14*, 41–51. [CrossRef]
49. Ishidate, K.; Creeger, E.S.; Zrike, J.; Deb, S.; Glauner, B.; MacAlister, T.J.; Rothfield, L.I. Isolation of Differentiated Membrane Domains from Escherichia coli and Salmonella typhimurium, including a Fraction Containing Attchments Sites between the Inner and Outer Membranes and the Murein Skeleton of the Cell Envelope. *J. Biol. Chem.* **1986**, *261*, 428–443. [CrossRef]
50. Olsen, R.W.; Ballou, C.E. Acyl Phosphatidylglycerol. *J. Biol. Chem.* **1971**, *246*, 3305–3313. [CrossRef] [PubMed]
51. Bishop, D.G.; Rutberg, L.; Samuelsson, B. The Chemical Composition of the Cytoplasmic Membrane of *Bacillus subtilis*. *Eur. J. Biochem.* **1967**, *2*, 448–453. [CrossRef]
52. Kamp, J.A.F.O.D.; Redai, I.; van Deenen, L.L.M. Phospholipid Composition of *Bacillus subtilis*. *J. Bacteriol.* **1969**, *99*, 298–303. [CrossRef] [PubMed]
53. Nickels, J.D.; Chatterjee, S.; Mostofian, B.; Stanley, C.B.; Ohl, M.; Zolnierczuk, P.; Schulz, R.; Myles, D.A.A.; Standaert, R.F.; Elkins, J.G.; et al. *Bacillus subtilis* Lipid Extract, A Branched-Chain Fatty Acid Model Membrane. *J. Phys. Chem. Lett.* **2017**, *8*, 4214–4217. [CrossRef]
54. Kawai, F.; Shoda, M.; Harashima, R.; Sadaie, Y.; Hara, H.; Matsumoto, K. Cardiolipin Domains in *Bacillus subtilis* Marburg Membranes. *J. Bacteriol.* **2004**, *186*, 1475–1483. [CrossRef]
55. Clejan, S.; Krulwich, T.A.; Mondrus, K.R.; Seto-Young, D. Membrane Lipid Composition of Obligately and Facultatively Al-kalophilic Strains of *Bacillus* spp. *J. Bacteriol.* **1986**, *168*, 334–340. [CrossRef]
56. Goldfine, H. *Lipids of Prokaryotes-Structure and Distribution*; Academic Press, Inc.: Cambridge, MA, USA, 1982; Volume 17, pp. 1–43.
57. Paul, S.; Chaudhuri, K.; Chatterjee, A.N.; Das, J. Presence of exposed phospholipids in the outer membrane of *Vibrio cholerae*. *J. Gen. Microbiol.* **1992**, *138*, 755–761. [CrossRef]
58. Lohia, A.; Chatterjee, A.N.; DAS, J. Lysis of Vibrio cholerae Cells: Direct Isolation of the Outer Membrane from Whole Cells by Treatment with Urea. *Microbiology* **1984**, *130*, 2027–2033. [CrossRef]
59. Pautsch, A.; Schulz, G.E. Structure of the outer membrane protein A transmembrane domain. *Nat. Struct. Mol. Biol.* **1998**, *5*, 1013–1017. [CrossRef] [PubMed]
60. Noureddini, H.; Teoh, B.C.; Clements, L.D. Densities of Vegetable Oils and Fatty Acids. *J. Am. Oil Chem. Soc.* **1992**, *69*, 1184–1188. [CrossRef]
61. Delgado, F.F.; Cermak, N.; Hecht, V.C.; Son, S.; Li, Y.; Knudsen, S.M.; Olcum, S.; Higgins, J.M.; Chen, J.; Grover, W.H.; et al. Intracellular Water Exchange for Measuring the Dry Mass, Water Mass and Changes in Chemical Composition of Living Cells. *PLoS ONE* **2013**, *8*, e67590.
62. Available online: https://pubchem.ncbi.nlm.nih.gov/ (accessed on 2 March 2025).
63. Available online: http://www.chemspider.com/ (accessed on 2 March 2025).
64. Jung, J.; Hong, S.J.; Kim, H.B.; Kim, G.; Lee, M.; Shin, S.; Lee, S.; Kim, D.J.; Lee, C.G.; Park, Y. Label-free non-invasive quantitative measurement of lipid contents in individual microalgal cells using refractive index tomography. *Sci. Rep.* **2018**, *8*, 6524. [CrossRef] [PubMed]
65. Romeo, D.; Girard, A.; Rothfield, L. Reconstitution of a Functional Membrane Enzyme System in a Monomolecular Film. *J. Mol. Biol.* **1970**, *53*, 475–490. [CrossRef]
66. Gul, B.; Ashraf, S.; Khan, S.; Nisar, H.; Ahmad, I. Cell refractive index: Models, insights applications and future perspectives. *Photodiagn. Photodyn. Ther.* **2021**, *33*, 102096. [CrossRef]
67. Beuthan, J.; Minet, O.; Helfmann, J.; Herrig, M.; Müller, G. The spatial variation of the refractive index in biological cells. *Phys. Med. Biol.* **1996**, *41*, 369–382. [CrossRef]
68. Johnsen, S.; Widder, E.A. The physical basis of transparency in biological tissue: Ultrastructure and the minimization of light scattering. *J. Theor. Biol.* **1999**, *199*, 181–198. [CrossRef]
69. Neidhardt, F.C. Escherichia coli and Salmonella Typhimurium Cellular and Molecular Biology. *Am. Soc. Microbiol.* **1987**, *1*, 3–6.
70. Merchante, R.; Pooley, H.M.; Karamata, D. A periplasm in *Bacillus subtilis*. *J. Bacteriol.* **1995**, *177*, 6176–6183. [CrossRef] [PubMed]
71. Marquis, R.E. Immersion Refractometry of Isolated Bacterial Cell Walls. *J. Bacteriol.* **1973**, *116*, 1273–1279. [CrossRef] [PubMed]

72. Fowles, G.R.; Lynch, D.W. *Introduction to Modern Optics*; Dover Publications: New York, NY, USA, 1989.
73. Pepino, R.; Calabrò, F.; Fella, P.; Tari, H.; Bile, A.; Nabizada, A.; Fazio, E. Bacteria Recognition: Neural Algorithms for Recognition. *submitted*.

**Disclaimer/Publisher's Note:** The statements, opinions and data contained in all publications are solely those of the individual author(s) and contributor(s) and not of MDPI and/or the editor(s). MDPI and/or the editor(s) disclaim responsibility for any injury to people or property resulting from any ideas, methods, instructions or products referred to in the content.